Available online at www.sciencedirect.com
ScienceDirect
Progress in Natural Science 18 (2008) 671–677
Progress in Natural Science
www.elsevier.com/locate/pnsc

High resolution imaging using scanning ion conductance microscopy with improved distance feedback control

Chao Li [a,*], Nicholas Johnson [a,1], Victor Ostanin [a], Andrew Shevchuk [b], Liming Ying [a], Yuri Korchev [b], David Klenerman [a,*]

[a] Department of Chemistry, University of Cambridge, Lensfield Road, Cambridge CB2 1EW, United Kingdom
[b] Division of Medicine, Imperial College London, MRC Clinical Sciences Centre, Hammersmith Campus, London W12 0NN, United Kingdom

Received 16 January 2008; accepted 18 January 2008

Abstract

Microscopy is an essential technique for observation on living cells. There is currently great interest in applying scanning probe microscopy to image-living biological cells in their natural environment at the nanometer scale. Scanning ion conductance microscopy is a new form of scanning probe microscopy, which enables non-contact high-resolution imaging of living biological cells. Based on a scanned nanopipette in physiological buffer, the distance feedback control uses the ion current to control the distance between the pipette tip and the sample surface. However, this feedback control has difficulties over slopes on convoluted cell surfaces, which limits its resolution. In this study, we present an improved form of feedback control that removes the contribution of up to the third-order slope from the ion current signal, hence providing a more accurate signal for controlling the distance. We show that this allows faster and lower noise topographic high-resolution imaging.

Keywords: Living biological cells; Scanning ion conductance microscopy; Distance feedback control

1. Introduction

Scanning ion conductance microscopy (SICM) first developed by Hansma et al. [1], is a method for high resolution non-contact imaging [2] of living biological cells [3] under physiological conditions. For almost two decades since its invention, SICM has been improved [4,5] and applied to imaging many types of small living cells, e.g., contracting cardiac myocytes [6], kidney epithelial A6 cells [7] and neuronal synapses [8]. SICM uses a distance feedback control to respond to dynamic changes as the pipette is scanned over the sample to obtain a topographic image. The input signal into the feedback control is the ion current and the output signal controls the distance between tip and sample surface. In order to improve the feedback control further it is necessary to provide a signal that only depends on the distance of the pipette from the sample surface and not the slope of the surface. If the feedback control signal also contains a contribution from the slope of the surface, then the correct distance from the surface cannot be determined and it will take a longer time to scan such a sample. To address this issue we developed a distance feedback control algorithm capable of removing the contribution of slope up to the third order. This algorithm was then used for SICM imaging with a significant improvement in image resolution.

* Corresponding authors. Tel.: +44 1223 336481; fax: +44 1223 336362.
E-mail address: dk10012@cam.ac.uk (D. Klenerman).
[1] This author contributed equally to this work.

1002-0071/$ - see front matter © 2008 National Natural Science Foundation of China and Chinese Academy of Sciences. Published by Elsevier Limited and Science in China Press. All rights reserved.
doi:10.1016/j.pnsc.2008.01.011

2. Method

2.1. Principle of SICM

The basic arrangement of SICM is shown in Fig. 1. SICM is based on an electrolyte-filled glass nanopipette which raster scans over the sample surface, and uses the ion current that flows between an electrode in the pipette and a bath electrode for feedback control of the pipette and sample distance. This tip-sample distance is maintained at the pipette inner radius during the scan, thereby allowing non-contact imaging of the cell surface in physiological buffer with a resolution determined by the pipette inner radius. Applying a constant voltage to the pipette, ion current flowing from the nanopipette decays rapidly as the nanopipette approaches the sample surface. The distance feedback control detects change in ion current, and adjusts the tip-sample distance to compensate. However, reduction in ion current is also due to other sources, such as ionic strength and conductivity change of solutions or partial blockage of the nanopipette, all of which will result in unwanted changes in pipette-sample separation. To address this issue, distance-modulation feedback control [9] was developed (Fig. 1b). This technique uses a driven vertical movement of the nanopipette (Δd) to generate a modulated signal that is present in the overall current. The modulated signal is detected and used in a more robust feedback control that can tolerate significant changes in ion current from unwanted sources. With distance-modulation feedback we have been able to continuously scan living cells for more than 24 h without loss of control [9].

Two pipette approach curves with non-modulated (DC) and modulated ion current measurements are shown in Fig. 2. These approach curves illustrate the dependence of both non-modulated current (I_{DC}) and modulated current (I_{MOD}) with the distance between pipette tip and sample surface. The I_{DC} is at the maximum when the pipette is a long way from the surface. In contrast, I_{MOD} is only generated when the tip senses the sample, i.e., at the distance of approximately one nanopipette tip radius from the sample surface, and increases dramatically as the tip approaches

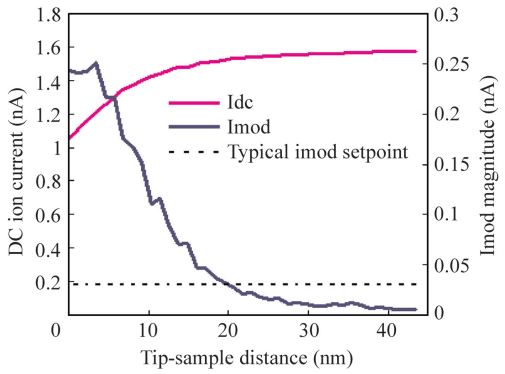

Fig. 2. DC and modulated approach curves for the SICM. Both ion current measurements were taken with a 75 nm inner diameter pipette vertically modulated by 10 nm. The dashed line shows the typical value of IMOD which is used as the setpoint for the feedback control.

the surface from that point. I_{MOD} reaches a maximum at the point that the pipette touches the surface whereas I_{DC} approaches a minimum due to the pipette blockage by the sample surface. In the distance-modulated feedback control mode, the optimal scanning distance is approximately one nanopipette inner tip radius from the surface which gives a modulated current (I_{MOD}) that stays in the same optimal range of 0.2–3% of I_{DC}. In this case, significant changes in the value of I_{DC}, e.g., ionic strength change or partial blockage of pipette will only induce a proportional change in I_{MOD} (from 1% to 2% of I_{DC}). Therefore, using I_{MOD} for distance feedback control is more reliable than using I_{DC}.

2.2. Principle of lock-in and improved distance feedback control

Lock-in detection [10] is a technique to recover signals in the presence of an extremely noisy background. SICM uses a lock-in algorithm to recover the modulated ion current from the overall ion current, which is usually very noisy. The processed signal of the lock-in is fed into the feedback control as its input signal. The lock-in algorithm uses a pair of digital reference modulation signals, Vx_{ref} and Vy_{ref}.

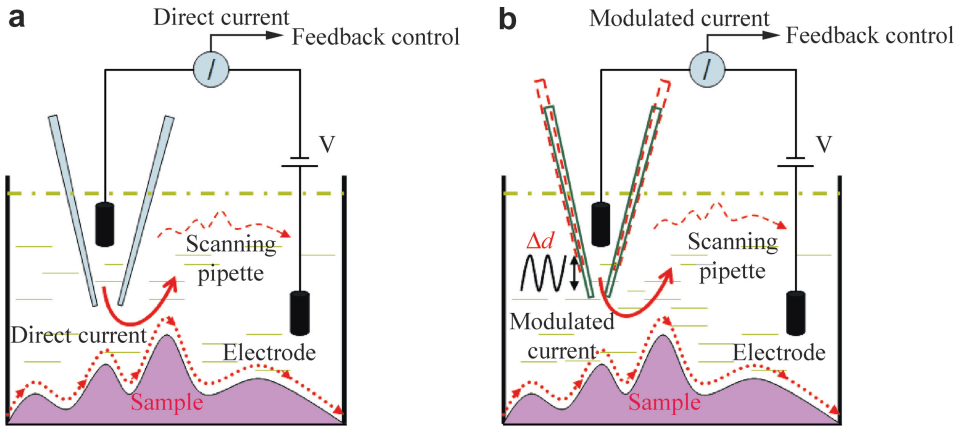

Fig. 1. Principle of SICM operation. (a) SICM non-modulated distance feedback control; (b) SICM modulated distance feedback control.

Vx_{ref} is used to drive the pipette modulation at a frequency F, resulting in an angular frequency $\omega = 2\pi F$:

$$Vx_{\mathrm{ref}}(t) = B\cos(\omega t) \quad (1)$$

$$Vy_{\mathrm{ref}}(t) = -B\sin(\omega t) \quad (2)$$

where B is the voltage amplitude.

The resulting modulated current is amplified by a current amplifier and produces an input voltage to the lock-in algorithm, V_{in}, given by:

$$V_{\mathrm{in}}(t) = V_{\mathrm{off}}(t) + A\cos(\omega t + \theta) + V_{\mathrm{noise}}(t) \quad (3)$$

where A is the amplitude of the modulating (AC) component voltage, θ is a phase-shift in the signal introduced mainly by the mechanical delay within the SICM instrument and $V_{\mathrm{off}}(t)$ is the DC component which is a smoothly varying background signal. Both are related by the approach curve [1].

Although in practice we use a digital signal processor (DSP), which is discrete in time, here, we present the continuous time equivalent (denoted by symbol "t") to provide a simpler description.

The SICM lock-in algorithm uses two-phase sensitive detectors [11] (PSD). One PSD multiplies components V_{in} with Vx_{ref}, and the other multiplies V_{in} with Vy_{ref}. The resulting two signals, after scaling and averaging over one or more modulation periods, are referred to as the X and Y channels of the lock-in and given by:

$$X = \langle V_{\mathrm{in}}(t) \cdot Vx_{\mathrm{ref}}(t)\rangle \cdot 2/B = A\cos(\theta) \quad (4)$$

$$Y = \langle V_{\mathrm{in}}(t) \cdot Vy_{\mathrm{ref}}(t)\rangle \cdot 2/B = -A\sin(\theta) \quad (5)$$

where $\langle f(t)\rangle$ denotes the averaging of $f(t)$ over n-modulation periods, as defined by $\frac{1}{2n\pi}\int_{-n\pi}^{n\pi} f(t)\mathrm{d}t$.

To make the formulae simpler here and below we use normalised time units so that $\omega = 1$. We also assume $t = 0$ at the middle of the averaging period, which is shifted to $n/2$ modulation periods back from the present time point. In our case, n is equal to 4.

The output of the lock-in, R, which is fed into the feedback control, is calculated using the root mean square (RMS) [12] of the X and Y channels:

$$R = \sqrt{X^2 + Y^2} = A \quad (6)$$

However, a problem arises when scanning over a sample that has convoluted surfaces. In this case, input voltage V_{in} is contaminated with significant slope components that are changing with time as the pipette scans over the sample. For a short interval of time during the scan we can approximate the input voltage, V_{in}, as a sum of sinusoidal functions (the result of modulation) and a polynomial of up to third order representing the slope of the sample. The noise of the measurement is assumed to be additive with zero mean value and not considered here for simplicity. Hence, the input voltage can be represented as follows:

$$V_{\mathrm{in}}(t) = V_{\mathrm{off}} + V_{1\mathrm{s}} \cdot t + V_{2\mathrm{s}} \cdot t^2 + V_{3\mathrm{s}} \cdot t^3 + A\cos(t + \theta) \quad (7)$$

where V_{off} is the offset, $V_{1\mathrm{s}}$, $V_{2\mathrm{s}}$ and $V_{3\mathrm{s}}$ are the first order (linear), second order (quadratic) and third order (cubic) slopes, respectively, and A is the amplitude of the fundamental modulation frequency. The second and higher-order harmonics of the fundamental modulation frequency appear due to the strong non-linearity of the approach curve but they have not been considered in this treatment for simplicity and because all the algorithms shown below are insensitive to these higher harmonics.

The input voltage $V_{\mathrm{in}}(t)$ processed by the two PSDs to calculate the X and Y channels of the lock-in is

$$X = \langle V_{\mathrm{in}}(t) \cdot Vx_{\mathrm{ref}}(t)\rangle \cdot 2/B = A\cos(\theta) + 4 \cdot V_{2\mathrm{s}} \quad (8)$$

$$Y = \langle V_{\mathrm{in}}(t) \cdot Vy_{\mathrm{ref}}(t)\rangle \cdot 2/B = A\sin(\theta) + 2 \cdot V_{1\mathrm{s}} + (32\pi^2 - 12) \cdot V_{3\mathrm{s}} \quad (9)$$

From Eqs. (8) and (9) above, the X and Y magnitudes contain the first, second and third order slope components. This may cause a serious problem in feedback control if these components are significant. In practice, with high-speed scanning over steep slopes we have found that the lock-in algorithm produces an incorrect and sometimes unstable signal for the feedback. In order to scan faster it is necessary to send the correct signal into the feedback control, without the contribution of the slope.

Below we modelled the signal for the pipette scanning over a hole as shown in Fig. 3, assuming that the z-position of the pipette is fixed and the pipette-surface distance changes as shown by the dark blue line. The distance feedback control is off. The pipette is modulated with an amplitude of 0.05 U of the pipette's radius around its position. The ion current signal shown by the red line was modelled by using a realistic approach curve function verified by experiment (data not shown). The light blue line shows the measured value of the lock-in output, R, which does not smoothly vary following the pipette-surface distance.

Due to the interference of the slope from the scanned topographic feature, a wavy component in R occurs, which may cause the wrong pipette-sample position to be

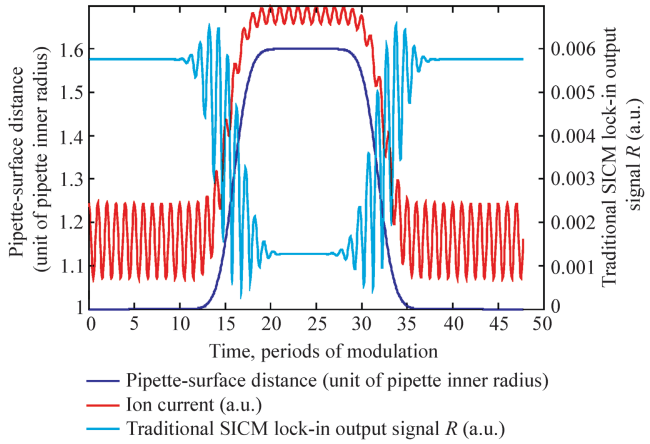

Fig. 3. Modelled traditional SICM lock-in signal when scanning over a topographic feature with the distance feedback control off. This is shifted forwards two periods for ease of presentation because the integration is performed between −2 and +2 periods.

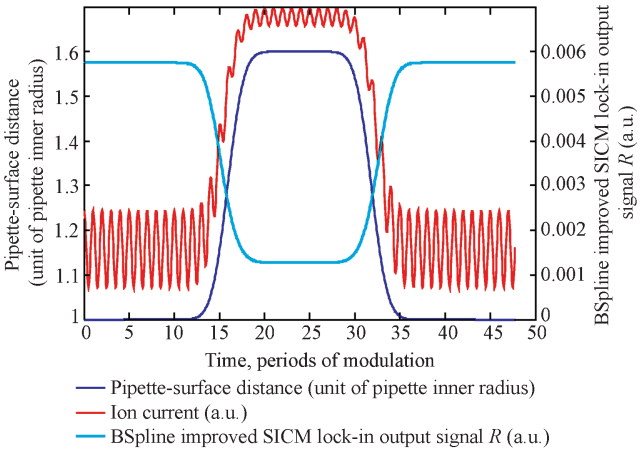

Fig. 4. Modelled BSpline improved SICM lock-in signal when scanning over a topographic feature with the distance feedback control off. This is shifted forwards two periods for ease of presentation because the integration is performed between −2 and +2 periods.

determined and may even cause the feedback, when switched on, to move briskly in the wrong direction leading to spikes in the image. Reducing the feedback gain will save the pipette from crashing but slow the scanning speed.

In order to remove these slope components, we have developed a lock-in algorithm using cubic B-wavelet functions. The B-wavelet is sinusoid and co-sinusoid modulated by the cubic BSpline function [13]. The BSpline function is used in spline theory and can also be described as the probability distribution function of the sum of four random uniformly distributed numbers over the interval $[-\pi, \pi]$, a scaled-up version is used to obtain the BSpline (t) as in the following formula:

$$\mathrm{Bspline}(t) = \begin{bmatrix} 4\left(\frac{4}{3} - 2\tau^2 + \tau^3\right) & \tau < 1 \\ \frac{4}{3}(2-\tau)^3 & 1 \le \tau < 2 \\ 0 & \tau \ge 2 \end{bmatrix} \tag{10}$$

where $\tau = \frac{t}{2\pi}$.

We multiply Vx_{ref} and Vy_{ref} with the BSpline(t) coefficient, giving new values, $Vx_{\mathrm{ref}}(t)'$ and $Vy_{\mathrm{ref}}(t)'$, given by:

$$Vx_{\mathrm{ref}}(t) = \mathrm{BSpline}(t) \cdot \cos(t) \tag{11}$$

$$Vy_{\mathrm{ref}}(t) = -\mathrm{BSpline}(t) \cdot \sin(t) \tag{12}$$

Note that the z-modulating signal remains unchanged as shown in Eq. (1).

We then multiplied V_{in} with $Vx_{\mathrm{ref}}(t)'$ and V_{in} with $Vy_{\mathrm{ref}}(t)'$, respectively. The resulting X' and Y', shown

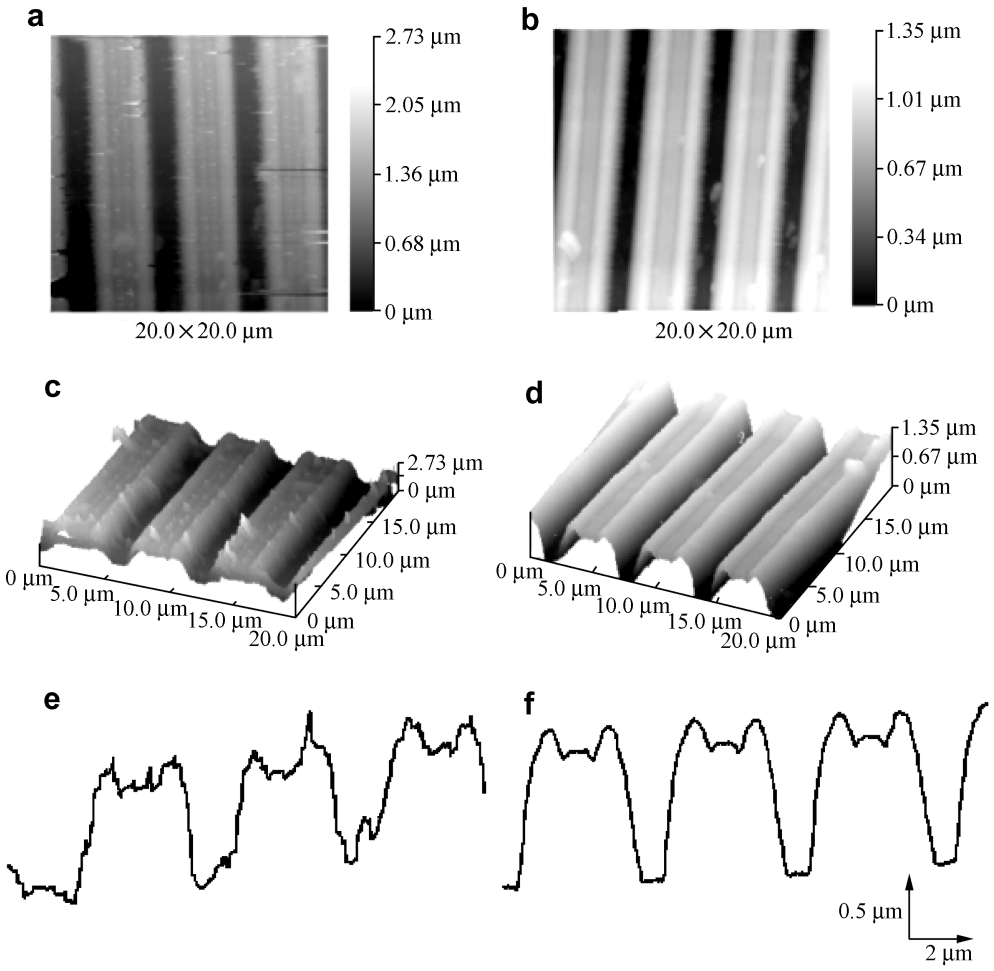

Fig. 5. SICM images of PDMS lines. (a and b) Images scanned with the old software and new improved software, respectively, (c and d) 3D surface topography of images (a and b), respectively, (e and f) a single horizontal line scan of the images (a and b), respectively.

below, do not contain interferences from the first, second or third order slope components.

$$X' = \langle V_{\text{in}}(t) \cdot Vx_{\text{ref}}(t) \rangle = A\cos(\theta) \quad (13)$$

$$Y' = \langle V_{\text{in}}(t) \cdot Vy_{\text{ref}}(t) \rangle = -A\sin(\theta) \quad (14)$$

Therefore, the lock-in output, *R,* given by Eq. (6), does not contain any slope components and the modulated distance feedback control is not sensitive to slope components up to the third order. Fig. 4 demonstrates that the spurious wavy interference on slopes became completely suppressed with the BSpline lock-in output, *R,* as shown by the light blue line, which smoothly varies following the pipette–surface distance (dark blue line).

2.3. Instrument

The basic arrangement of the SICM for imaging living cells is similar to the previous work [14,15]. The sensitive probe of the SICM is a glass nanopipette filled with electrolyte. The nanopipettes were made from 1.00-mm outer diameter, 0.58-mm inner diameter borosilicate or 0.50-mm quartz microcapillaries (Intracel, Herts, UK) on a laser-based Brown–Flaming puller (model P-2000, Sutter Instrument Company, San Rafael, USA). The nanopipettes and the bath were filled with the same electrolyte, usually physiological buffer or growth media. The inner diameter of borosilicate nanopipettes was measured for a few metal coated-pipettes using scanning electron microscopy and found to be normally ~75 nm and for quartz was normally ~25 nm. The samples were placed on petri dishes.

A voltage was applied between a silver chloride electrode in a pipette and a similar electrode in the bath to create the ion current used as the input signal to the feedback control. The pipette height was modulated using a 25-μm travel range piezo actuator (Physik Intrumente, P-753.21C, Germany). The frequency of modulation ranged from 200 to 1025 Hz. The resulting modulated ion current signal was amplified with a patch clamp amplifier (Axon Instruments, AxoPatch 200B, USA) and then processed using a digital signal processor (Texas Instruments, SBC 6711, USA) running the lock-in and feedback control algorithms. The sample was raster scanned underneath the pipette using a 100-μm travel X–Y piezo actuator (Physik Intrumente, P-621.2CL, Germany). The scanning apparatus was placed on an optical microscope (Nikon TE200, Japan) for coarse alignment and visualisation. The

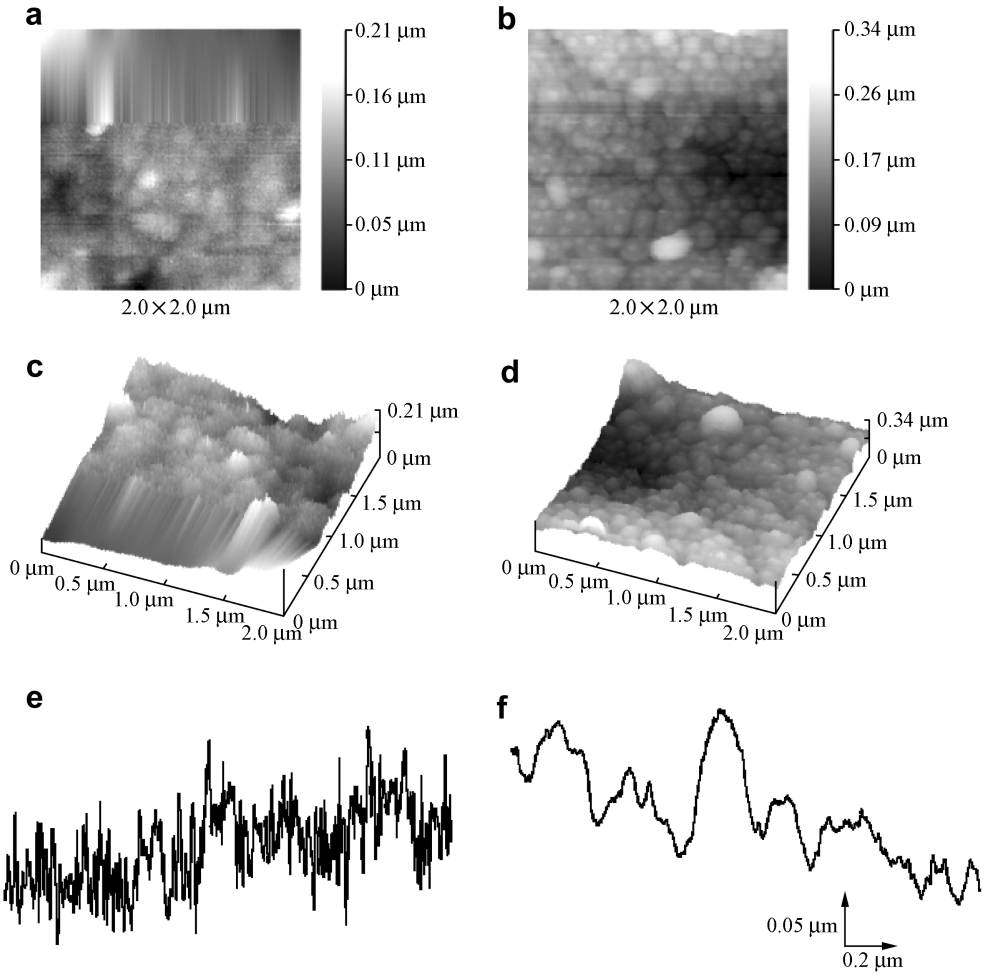

Fig. 6. SICM images of gold on carbon. (a and b) images scanned with the old software and new improved software, respectively, (c and d) 3D surface topography of images (a and b), respectively, (e and f) a single horizontal line scan of the images (a and b), respectively.

microscope was positioned on a vibration isolation system (Minus K Technology 100BM-8, USA).

For the model-sample images, coarse movement in all axes was provided by 25 mm travel DC stepper motors (Physik Intrumente, M-112.1DG, Germany). The z-axis piezo was mounted to the DC motor which was connected to the side of a small box. The DC motors for X–Y movement were mounted to a shelf in the box, and the X–Y piezo driving the sample dish was attached to the motors. For the cell images, the z-axis piezo with the pipette was mounted to a plate that moved vertically using a 25-mm travel micrometer. The x–y axis piezo and sample dish were mounted to translation stages controlled by similar micrometers.

2.4. Samples

2.4.1. PDMS lines

A Polydimethylsiloxane (PDMS) stamp was prepared following a literature procedure [16]. Briefly, a silicon master (1.2 by 1.2 cm) patterned with microscale features by standard photolithography was treated with a 1H, 1H, 2H, 2H-perfluorodecyltrichlorosilane for 2 h to produce a non-sticky perfluorinated coating. The master was placed in a plastic weighing boat and covered with 2 ml of polydimethylsiloxane pre-polymers (Sylgard®184 silicone elastomer, 10:1 mixture of the two parts, Dow Corning, USA). It was then cured in an oven at 80 °C for 12 h. The master was separated from the cured PDMS stamp with a pair of tweezers. The stamp was cut into $\sim 1 \times 1\ cm^2$ square, rinsed with methanol and dried over a stream of N2 before being used for SICM imaging.

2.4.2. Gold on carbon

A low-kV unmounted gold on carbon SEM specimen was purchased (Ted Pella Inc, USA, S168UZ). The sample was fixed to a Petri dish using acetoxy silicone (Dow Corning, USA). The gold on carbon sample has lateral feature sizes ranging from less than 30 nm up to 500 nm.

2.4.3. Kidney epithelial A6 cells

A single A6 cell line (Katholieke Universiteit, Leuven, Belgium) was used in the experiments, which were carried out between 127 and 134 passages. Cells were cultured as described previously [17] on membrane filter inserts (23 mm diameter, 0.4 μm pore, 1.6×10^6 pores/cm^2) or Petri dishes (Falcon) (Becton Dickinson Labware, Oxford, UK). Briefly, cells were grown and kept in a 1:1 mixture of modified Ham's F-12 medium and Leibovitz's L-15 medium (Gibco), modified to contain 105 mmol/l NaCl and 25 mmol/l $NaHCO_3$. The mixture was supplemented with 10% fetal calf serum (FCS), 200 mg/ml streptomycin, and 200 U/ml penicillin (Gibco). Cells were maintained at 28 °C in an atmosphere of humidified air plus 1% CO_2.

3. Results and discussion

We scanned a number of model samples, with different topographic features, using the improved distance feedback control and compared the results with the old control software using the traditional lock-in. We first scanned the PDMS lines with a 20 μm by 20 μm square (Fig. 5). The new image Fig. 5b is clearly less noisy than the image scanned with the old software Fig. 5a. From the three-dimensional topography of the two images, many more

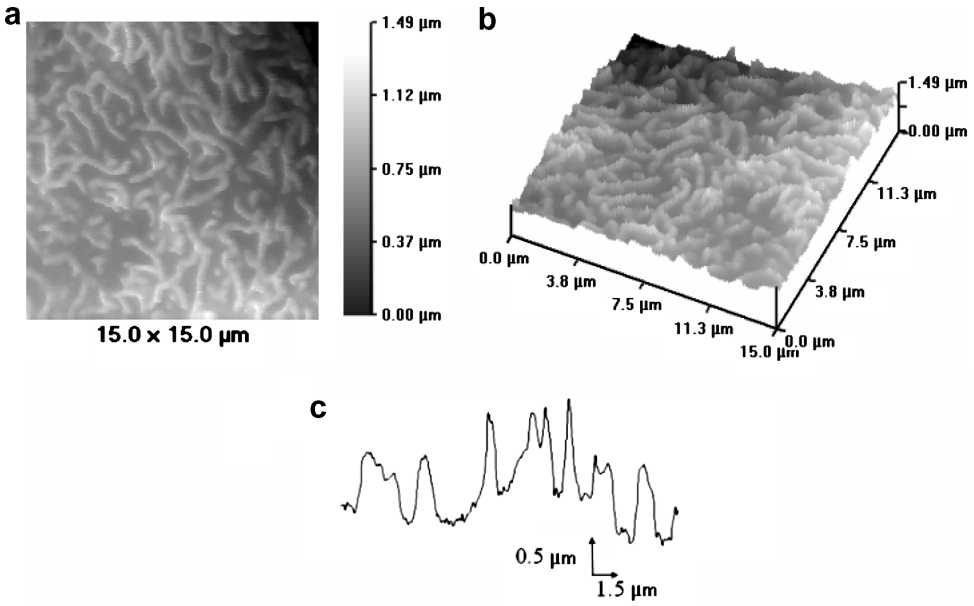

Fig. 7. SICM images of kidney epithelial A6 cells. (a) image scanned with the new improved software, (b) 3D surface topography of image A, (c) a single horizontal line scan of the image A.

spikes were present in Fig. 5c, which were not the topography of the surface but artefacts introduced by the old scan software due to the incorrect sensing of the surface. With Fig. 5d, the new improved software has no artificial spike from scanning the sample surface. From a horizontal-line scan, it can be seen that the line topography is much less noisy and contains no spike in the new improved software (Fig. 5f) when compared to the old SICM software (Fig. 5e).

A significant improvement in resolution was found when scanning the gold on carbon with a 2 μm by 2 μm scan as shown in Fig. 6. The results indicate that smaller features, roughly 10-nm can be resolved with the new software (Fig. 6b), which are not visible from the image with the old software (Fig. 6a). The scan times were both approximately 37 min. From the line scan, we can see that the topography is less noisy and represents the true topography more accurately in Fig. 6f.

We then scanned fixed kidney epithelial A6 cells as shown in Fig. 7. Small surface structure microvilli [18] can be more clearly identified using the improved software (Fig. 7a). From the line scan, we can see that it is also possible to obtain accurate topography, as shown in Fig. 7c. These images show that high quality topographic images of cells can be obtained using these software improvements.

From the above examples of SICM imaging, we have demonstrated a significant improvement in image quality using an improved distance feedback control that removes the contribution of slope from the feedback control signal. This will also allow improvements in image speed since it is now possible to obtain a topographic image with the required signal to noise in a reduced time. This is a significant step in realising our goal of fast high-resolution imaging of living cells.

Acknowledgements

This work was supported by the United Kingdom Biotechnology and Biological Sciences Research Council (BBSRC) and Medical Research Council (MRC). We thank Dr. Dejian Zhou and Dr. P. DeSmet for kindly providing the PDMS stamp and single A6 cell-line sample, respectively. We are grateful to Dr. Andreas Bruckbauer and Joe Piper of the Klenerman group for constructive criticism in the preparation of this manuscript.

References

[1] Hansma PK, Drake B, Marti O, et al. The scanning ion-conductance microscope. Science 1989;243(4891):641–3.
[2] Ying LM, Bruckbauer A, Zhou DJ, et al. A new tool for high resolution bioimaging and controlled deposition of biomolecules. Phys Chem Chem Phys 2005;7:2859–66.
[3] Korchev YE, Milovanovic M, Bashford CL, et al. Specialized scanning ion-conductance microscope for imaging of living cells. J Microsc 1997;188:17–23.
[4] Prater GB, Hansma PK, Tortonese M, et al. Improved scanning ion-conductance microscope using microfabricated probes. Rev Sci Instrum 1991;62:2634–8.
[5] Proksch R, Lai R, Hansma PK, et al. Imaging the internal and external pore structure of membranes in fluid: tapping mode scanning ion conductance microscopy. Biophys J 1996;71:2155–7.
[6] Gorelik J, Ali NN, Shevchuk AI, et al. Functional characterization of embryonic stem cell-derived cardiomyocytes using scanning ion conductance microscopy. Tissue Eng 2006;12:657–64.
[7] Gorelik J, Zhang Y, Shevchuk AI, et al. The use of scanning ion conductance microscopy to image A6 cells. Mol Cell Endocrinol 2004;217:101–8.
[8] Gorelik JV, Benton DCH, Monaghan A, et al. Studying of neuronal synapses by scanning ion conductance microscopy. Biophys J 2005;88:305A.
[9] Korchev YE, Bashford CL, Milovanovic M, et al. Scanning ion conductance microscopy of living cells. Biophys J 1997;73:653–8.
[10] Wolfson R. The lock-in amplifier: a student experiment. Am J Phys 1991;59(6):569–72.
[11] Summers CP. The US Patent, 4 422 176, 1983.
[12] Kenney JF, Keeping ES. Mathematics of statistics. 3rd ed. Princeton: Van Nostrand; 1962, 59–60.
[13] Masami U, Lodha S. Wavelets: an elementary introduction and examples. University of California at Santa Cruz Technical Report, UCSC-CRL-94-47, 1995. pp. 23–8.
[14] Shevchuk AI, Frolenkov GI, Sánchez D, et al. Imaging proteins in membranes of living cells by high-resolution scanning ion conductance microscopy. Angew Chem Int Ed 2006;45:2212–6.
[15] Shevchuk AI, Gorelik J, Harding SE, et al. Simultaneous measurement of $Ca2^{+}$ and cellular dynamics: combined scanning ion conductance and optical microscopy to study contracting cardiac myocytes. Biophys J 2001;81:1759–64.
[16] Zhou D, Bruckbauer A, Ying LM, et al. Building three-dimensional surface biological assemblies on the nanometer scale. Nano Lett 2003;3:1517–20.
[17] Kemendy AE, Kleyman TR, Eaton DC. Aldosterone alters the open probability of amiloride-blockable sodium channels in A6 epithelia. Am J Physiol 1992;263:C825–37.
[18] Gorelik J, Shevchuk AI, Frolenkov GI, et al. Dynamic assembly of surface structures in living cells. Proc Natl Acad Sci 2003;100:5819–22.